

Nested Metamaterials for Wireless Strain Sensing

Rohat Melik, *Student Member, IEEE*, Emre Unal, Nihan Kosku Perkgoz, Brandon Santoni, Debra Kamstock, Christian Puttlitz, and Hilmi Volkan Demir, *Member, IEEE*

Abstract—We designed, fabricated, and characterized metamaterial-based RF-microelectromechanical system (RF-MEMS) strain sensors that incorporate multiple split ring resonators (SRRs) in a compact nested architecture to measure strain telemetrically. We also showed biocompatibility of these strain sensors in an animal model. With these devices, our bioimplantable wireless metamaterial sensors are intended, to enable clinicians, to quantitatively evaluate the progression of long-bone fracture healing by monitoring the strain on the implantable fracture fixation hardware in real time. In operation, the transmission spectrum of the metamaterial sensor attached to the implantable fixture is changed when an external load is applied to the fixture, and from this change, the strain is recorded remotely. By employing telemetric characterizations, we reduced the operating frequency and enhanced the sensitivity of our novel nested SRR architecture compared to the conventional SRR structure. The nested SRR structure exhibited a higher sensitivity of 1.09 kHz/kgf operating at lower frequency compared to the classical SRR that demonstrated a sensitivity of 0.72 kHz/kgf. Using soft tissue medium, we achieved the best sensitivity level of 4.00 kHz/kgf with our nested SRR sensor. Ultimately, the laboratory characterization and *in vivo* biocompatibility studies support further development and characterization of a fracture healing system based on implantable nested SRR.

Index Terms—Biocompatibility, metamaterial, nested SRR, remote sensing, resonance frequency, sensitivity, split ring resonator (SRR), strain, telemetric.

I. INTRODUCTION

THE ABILITY to telemetrically measure strain is important in many aspects of daily life. But such a task brings about important challenges. In many sectors such as in civil engineering, measuring the strength of materials (e.g., concrete), remotely in real time, will help us to understand their transient

Manuscript received June 5, 2009; revised June 29, 2009 and August 27, 2009. First published December 28, 2009; current version published April 7, 2010. This work was supported in part by the Turkish National Academy of Sciences Distinguished Young Scientist Award and European Science Foundation European Young Investigator Award Programs, and The Scientific and Technological Research Council of Turkey under Projects EEEAG 104E114, 106E020, 107E088, 107E297, 109E002, and 109E004. This work is also supported by a grant from the United States National Institutes of Health (NIH) 5R01EB010035-02.

R. Melik, E. Unal, and N. K. Perkgoz are with the Department of Electrical and Electronics Engineering, Nanotechnology Research Center, and Institute of Materials Science and Nanotechnology, Bilkent University, 06800 Ankara, Turkey (e-mail: rohat@ee.bilkent.edu.tr; unale@bilkent.edu.tr; kosku@bilkent.edu.tr).

B. Santoni, D. Kamstock, and C. Puttlitz are with the Orthopedic Bioengineering Research Laboratory, Department of Mechanical Engineering and School of Biomedical Engineering, Colorado State University, Fort Collins, CO 80523 USA (e-mail: bgsant@engr.colostate.edu; Debra.Kamstock@Colostate.Edu; puttlitz@engr.colostate.edu).

H. V. Demir is with the Department of Electrical and Electronics Engineering, the Department of Physics, Nanotechnology Research Center, and Institute of Materials Science and Nanotechnology, Bilkent University, 06800 Ankara, Turkey (e-mail: volkan@bilkent.edu.tr).

Color versions of one or more of the figures in this paper are available online at <http://ieeexplore.ieee.org>.

Digital Object Identifier 10.1109/JSTQE.2009.2033391

structural behavior better (e.g., before and after an earthquake). Real-time measurement of the flexural rigidity of aircraft components during service in avionics is also an important application of telemetric strain sensing. Another unrealized, yet critical, application area is human medicine.

One important clinical issue in which we are currently interested is objectively monitoring the healing processes of fractured long bones [1]. Orthopedic extremity injuries currently present a large medical and financial burden to both the United States and worldwide communities, as can be seen in [2]. Severely comminuted-fracture patterns, commonly seen in high-energy fractures, are difficult to treat due to the inherent absence of mechanical support by the native osseous tissue. In these cases, the implanted hardware (intramedullary rods, bone plates, screws, etc.) must assume the total mechanical load in the early postoperative term, which frequently results in an aberrant course of healing and the onset of delayed union or nonunion. The most common treatment for these complications is additional surgery. These types of orthopedic injuries require prolonged time before patients return to full activity [3].

Approximately six million long bone fractures are reported per annum in the United States. Surprisingly, approximately 10% of these fractures do not heal properly. Though the exact mechanism through which the healing progression becomes impaired is poorly understood, many of these nonunions or pseudoarthroses result when there is a severe or comminuted condition that does not proceed through a stabilized (intramembranous ossification) healing pathway [4]. Currently, clinicians may monitor healing visually by radiographs, and may examine the mechanical condition of the union through manually bending the bone at the fracture [5]. However, the course of aberrant fracture healing is not easily diagnosed in the early time period when standard radiographic information of the fracture site is not capable of discriminating the healing pathway. The manual assessment of fracture healing is also subjective and, therefore, inadequate as a diagnostic tool in the early stages of healing, as shown in [6].

It has been shown in animal models that healing is critically important in the early time period. Animal studies have demonstrated that the callus and bone assume an increasing proportion of the load as healing proceeds, reducing the load carried by the implanted hardware [1]. However, to date, many of the technologies that seek to exploit this bone-implant load-sharing phenomena have been considered too large in dimension or involve implantation of an associated power supply. Previous investigations have been successful in determining forces in the hip [7]–[9], spine [10]–[12], and femur [13], [14]. However, due to the relatively large size of the sensors and associated hardware (signal conditioning, modulation, etc.), most of the aforementioned telemetry systems have been implanted insidejoint

replacement components or bulky internal fixators. The result is that these devices have produced data that have been useful in the understanding of bone-implant loading, but not been advantageous for large-scale implementation, as diagnostic and prognostic tools. Also, due to the complexity of the designs and requisite interconnectivity, manufacture of these systems could only be performed on a custom basis. The resulting expense could not justify their large-scale manufacture.

To overcome the aforementioned shortcomings, we have developed RF-microelectromechanical system (MEMS) strain sensors that take advantage of the recent advances in metamaterials. To date, metamaterials have been extensively investigated and exploited for various applications [15]–[26]. In the previous literature, some of these applications include achieving negative refraction [18]–[21], obtaining plasmons using nanowires [22], making metamaterial antennas [23], focusing light [24], cloaking [25], and building superlenses [26]. For metamaterials, sensing opens up a new direction where metamaterials may provide unique benefits.

These split ring resonator (SRR)-based sensors are passively powered devices (with no implantable power source), which we implement to monitor the surface bending strains on implanted fracture fixation hardware. Another important feature of these wireless sensors is that they do not require an internal–external physical connection to sense and transmit *in vivo* biological data. Finally, the miniaturization of these metamaterial-based sensors allows for their use in various implant applications that otherwise would not be possible. As the SRR-based sensor displays a characteristic resonance frequency under no load, by measuring the magnitude of operating frequency shift under applied load, we are able to delineate the bending strain incurred in the fixation hardware and intend to relate this information to the progression of fracture healing.

For the sensing operation, four criteria are important and demonstrate the quality of the sensor. First, the sensor must have a low enough operating frequency (subgigahertz range) to avoid the background absorption of soft tissue. This poses a significant challenge as conventional fracture fixation devices have limited area to which the sensors can be affixed, and such reduced space tends to increase the operating frequency of the sensor. This, in turn, undesirably increases the background absorption of human body (soft tissue). At higher frequencies, the soft tissue limits the penetration depth of electromagnetic waves. Therefore, it is required to maintain a small layout of the sensor while decreasing its operating frequency as much as possible.

Second, the sensors must emit a strong and measurable read-out signal with sharp enough resonance behavior (high enough Q -factor) to accurately track the shift in transmission spectra. The third criterion pertains to the linearity of sensing, which is related to the quality factor of the sensor. A higher Q -factor leads to a higher SNR, which reduces errors in the measurement (e.g., from the network analyzer) and decreases the non-linearity error. The fourth criterion is sensor sensitivity. Since there are a limited number of data points in one frequency scan of the network analyzer, it is easier to resolve smaller shifts in the transmission spectra in response to the externally applied load when the sensitivity is higher. With the same

level of induced strain, higher sensitivity yields larger shifts in transmission.

Metamaterials provide the ability to make better wireless sensors compared to conventional RF structures (e.g., spiral coils) because of their advantages over conventional structures with respect to four criteria listed earlier. The benefits of SRRs in telemetric sensing mainly stem from their unique structure, which features gaps (splits). Because of these gaps, SRRs exhibit lower resonance frequencies per unit area compared to spiral coils. This is critically important for bioimplant strain sensing within a limited space and in soft tissue environment. Furthermore, SRRs yield deeper and sharper dips, at resonance in their transmission spectra, compared to the spiral structures. The gaps of an SRR have much higher electric field density, which makes the resonance stronger and leads to a higher Q -factor, and, in turn, a higher SNR. This makes the SRR sensor more linear compared to the spiral coil sensor. As a final consequence of gap presence in the SRRs when an external load is applied, the change in the additional capacitance further shifts the operating frequency, making the SRR more sensitive compared to the spiral structure. In our previous work as such, we used a single SRR structure in our strain sensor [27].

In this paper, we fabricate and characterize nested metamaterial-based strain sensors that incorporate multiple SRRs in a compact nested architecture on a single chip to significantly achieve enhanced sensitivity in telemetric sensing. This architecture introduced for implant sensing substantially features more gaps compared to the structure of a conventional SRR. This decreases the operating resonance frequency of the resulting nested SRR sensor compared to the classical SRR sensor. Moreover, when the external load is applied, the capacitance of our nested SRR sensor is changed to a greater degree than the classical SRR, resulting in larger shifts in the transmission spectrum. This makes the nested SRR more sensitive than classical SRR in sensing.

Here we present the design, fabrication and characterization of our nested-metamaterial based RF-MEMS strain sensors, and compare the telemetric sensing operation of the classical SRR and nested SRR based sensors in telemetric sensing. Further, we characterize the site-specific biocompatibility and wound-healing response elicited against these sensors in a small animal model. Finally, we present the first proof-of concept telemetric demonstration of these nested SRR sensors using soft tissue *in vitro*.

II. DESIGN AND FABRICATION

Fig. 1(a)–(c) shows schematics of three designs of conventional SRRs, with two gaps (in two turns) in Fig. 1(a) (classical SRR), with a single gap (in one turn) in Fig. 1(b), and with four gaps (in four turns) in Fig. 1(c), respectively. Here, increasing the number of turns decreases the operating resonance frequency because of the increased number of gaps, and thus, increased capacitance. However, the total possible reduction in the resonance frequency is limited by the space available on the chip, as each turn takes up a considerable amount of space. To make a compact sensor, we propose nesting of SRRs that share the same sides except where the gap is located, as depicted in Fig. 1(d)

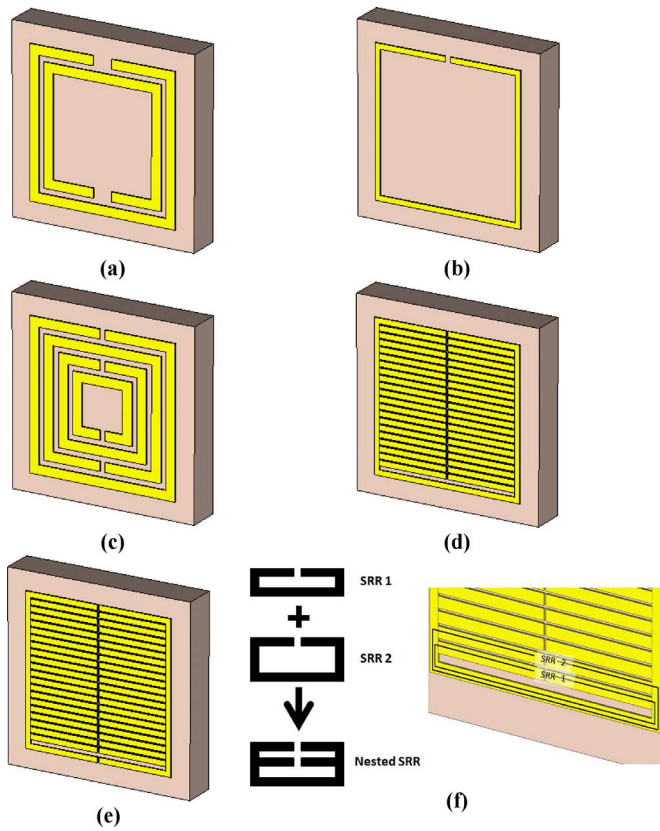


Fig. 1. SRR with (a) two turns (classical SRR), (b) one turn, and (c) four turns. (d) Nested SRR architecture. (e) Comb-like structure. (f) Zoom-in view of nested SRR.

(nested SRR). With many more gaps available in the nested SRR, the resonance frequency is further reduced, consequently resulting in an increase in sensor sensitivity.

A key feature of the nested architecture is the connected bottom line of the RF structure, which confers continuity in our nested design. For comparison, Fig. 1(e) shows a pair of comb-like structures. These comb-like structures yield undesirably high resonance frequencies (even higher than that of the classical SRR) due to the discontinuous bottom line. As can be seen in the zoom-in view of the nested SRR in Fig. 1(f), there are many SRRs nested together. These SRRs are added together with the same continuous bottom line, being the only difference with respect to Fig. 1(e).

For the classical SRR, we denote the total length of the outer coil as L_{out} , total length of the inner coil as L_{in} , width of the outer coil as w_{out} , width of the inner coil as w_{in} , spacing across the gap of the outer coil as s_{out} , and spacing across the gap of the inner coil as s_{in} . These parameters are depicted in Fig. 2(a). In the context of a design with fixed chip size (constant L_{out}), increasing L_{in} decreases the resonance frequency. But making L_{in} too much closer to L_{out} decreases Q -factor due to the increased parasitic capacitance. Increasing L_{in} increases the capacitance between substrate and metal (C_{diel}), decreasing the resonance frequency. Increasing w_{in} and w_{out} increases the capacitance between gaps (C_{gap}) as well as C_{diel} , which decreases the resonance frequency. Increasing s_{in} and s_{out} decreases C_{gap} , thus, increasing the resonance frequency.

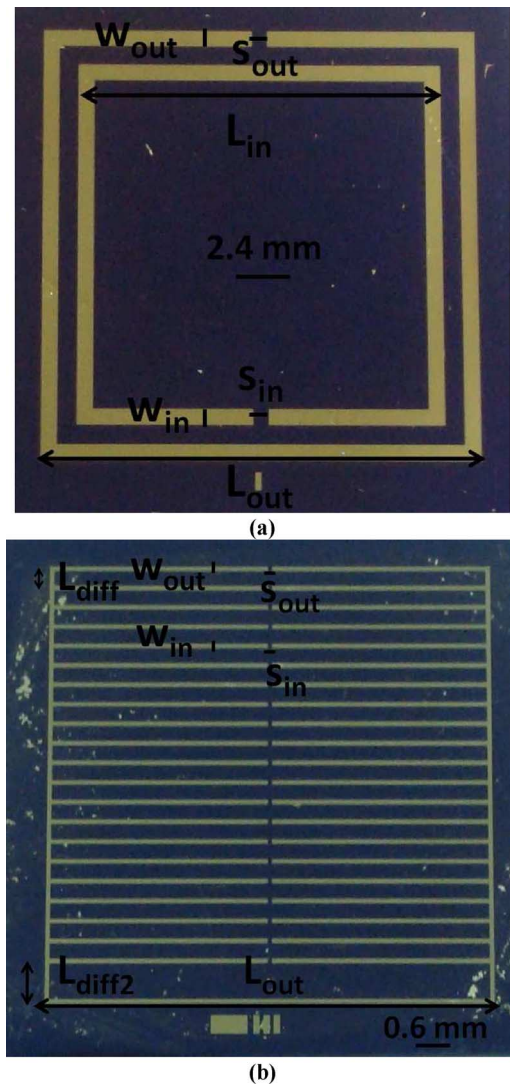


Fig. 2. Plain view pictures of (a) the classical SRR structure and (b) nested SRR structure.

The design parameters of the nested SRR are shown on a fabricated sample in Fig. 2(b). L_{diff} is the distance between the combs, and L_{diff2} is the distance between the bottom line and the bottom comb teeth. The width of the top comb teeth is w_{out} , and the width of the nested comb teeth is w_{in} . The spacing across the gap of the top comb teeth is s_{out} and that of the others is s_{in} . L_{out} is the total length of the structure. For the design parameters, the same conditions, as in classical SRR, apply in general. Increasing w_{in} and w_{out} decreases the resonance frequency. Increasing s_{in} and s_{out} increases the resonance frequency. If the width is much greater than the spacing, then the parasitic capacitance dominates, so the Q -factor decreases. Therefore, we carefully choose the ratio of the width to the spacing.

The most important parameter for determining the resonance frequency of the nested SRR is the number of comb teeth (N) in the design. As N increases, both C_{gap} and C_{diel} increase, thus decreasing the resonance frequency. Another parameter of interest in the nested SRR is L_{diff} . If we increase L_{diff} , then we decrease N . Subsequently, C_{gap} and C_{diel} are decreased, thereby

TABLE I
PARAMETERS OF CLASSICAL SRR

L_{out} (mm)	L_{in} (mm)	w_{out} w_{in} (mm)	s_{out} s_{in} (mm)	t_{film} (μm)	t_{metal} (μm)
22.2	18.6	0.8	0.8	0.1	0.1

TABLE II
PARAMETERS OF NESTED SRR

L_{out} (mm)	w_{out} w_{in} (mm)	s_{out} s_{in} (mm)	L_{diff} (mm)	L_{diff2} (mm)	t_{film} (μm)	t_{metal} (μm)	N
22.2	0.2	0.2	0.8	1.8	0.1	0.1	20

increasing the resonance frequency. However, L_{diff} should be greater than or equal to the width, otherwise the parasitic capacitance dominates. L_{diff2} is another important parameter. We decrease L_{diff2} as much as possible to decrease the resonance frequency, since our goal is to maximize N . If L_{diff2} is increased, then N is decreased. Therefore, C_{gap} and C_{diel} are decreased and the resonance frequency is increased. We make L_{diff2} greater than or equal to $2L_{diff} + w_{in}$ so that we do not ruin the sequence of the combs, and the parasitic capacitance does not dominate to decrease Q -factor.

The dielectric layer is also an important factor in our design. To have sufficient capacitance between the metal and the substrate, which serves as the distributed capacitance, we used a dielectric layer with a high dielectric constant [28]. On the other hand, to minimize the loss, a low-loss dielectric is required. Therefore, Si_3N_4 with a dielectric constant of eight and a loss tangent of 5×10^{-4} was chosen as the dielectric film to satisfy these conditions. Its film thickness was set to $0.1 \mu\text{m}$ to confer maximum capacitance over the minimum area.

The metal type and substrate used in the design are also critical, particularly for biocompatibility. We used Au as the metal layer and Si as the substrate. We also chose Si_3N_4 as the dielectric layer because it is biocompatible [28]. For the fabrication process, we first deposited $0.1\text{-}\mu\text{m}$ -thick Si_3N_4 onto our silicon substrate by plasma-enhanced chemical vapor deposition (PECVD). Then, by using standard lithography, metal evaporation, and lift-off, we deposited and patterned a $0.1\text{-}\mu\text{m}$ -thick Au film to make our sensors. The design parameters for the optimized classical SRR and the optimized nested SRR used in this paper are provided in Tables I and II.

III. EXPERIMENTAL CHARACTERIZATION

In this section, we characterized differences in telemetric strain-sensing ability between the classical SRR- and nested SRR-based sensors. We then evaluate the biocompatibility of our sensors over a six-month time period in a small animal model. Finally, we demonstrated telemetric operation in soft tissue using our nested SRR sensor as a first proof-of-concept demonstration for implant applications.

A. Comparison of Classical and Nested SRR Strain Sensors

We experimentally characterized the metamaterial-based sensors using a custom-design mechanical testing setup. In this pa-

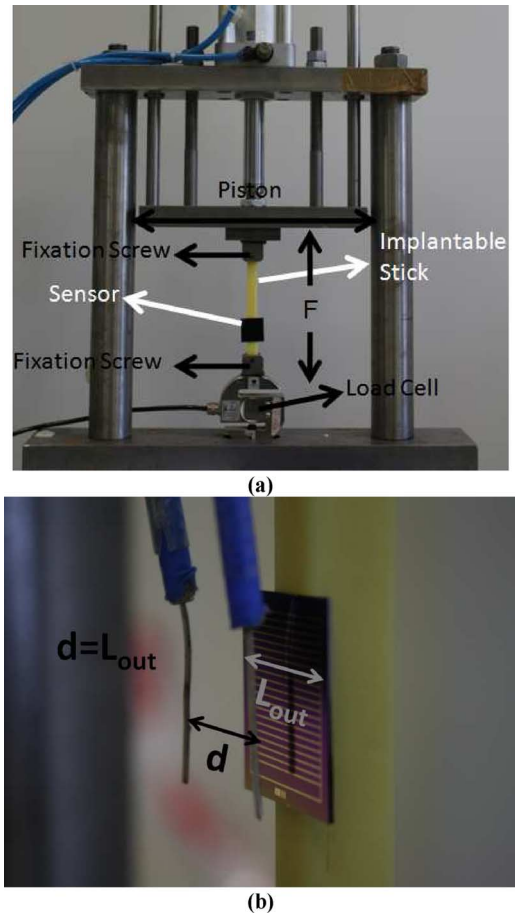


Fig. 3. (a) Mechanical apparatus and (b) coaxial probe antennas.

per, a uniaxial traction force was applied in a controlled manner to a polyamide beam rigidly coupled to a load cell and actuator, as shown in Fig. 3(a). Using this apparatus constructed at Bilkent University, loads were incrementally applied up to 300 kgf. The classic SRR and the nested SRR sensors were rigidly affixed to the polyamide beams with hard epoxy prior to testing.

Antennae made of coaxial probes with the same ground to decrease the noise during characterization were used to measure the change in RF spectrum of the loaded sensors during testing [see Fig. 3(b)]. The length of these probes was set to 2.5 cm, which was comparable to the size of our sensors. Because our sensors are small in size, i.e., $\lambda_o/30 - \lambda_o/25$, in comparison to their operating wavelength, it was rather difficult to use standard antennas with sizes comparable to our sensors to measure their transmission spectra. The distance between these probe antennas was set equal to L_{out} , and they were placed 0.5 cm away from the sensor, as shown in Fig. 3(b). In this configuration, the best signal is obtained with the probes parallel to the sensor. All these distance parameters were kept fixed throughout the calibration process and characterization process. For calibration purposes, the transmission of the polyamide beam was measured first with no sensor chip attached. Subsequently, the same measurement was repeated with the sensor attached under no load, and then, also following application of discrete tensile

loads. Transmission spectra referenced relative to the no-sensor condition were obtained as a function of the applied load.

Relative transmission spectra (in decibel) are presented in Figs. 4 and 5 for the classical SRR and nested SRR sensors, respectively, with respect to the case of no sensor in semilog scale. Under no load, the operating frequency of the classic SRR was 529.8 MHz. At this point, the size of this classical SRR sensor corresponded to $\lambda_o/25.5$. With the applied load, the operating frequency decreased, as seen in Fig. 4(a) and (b). Under the applied tensile load, the gaps of SRR are decreased, hence, C_{gap} is increased. Also the dielectric area between substrate and metal layer is increased, thus C_{diel} is increased [29]. Fig. 4(c) plots the operating frequency shift (with respect to the case of no load) as a function the applied load and indicates a sensitivity of 0.723 kHz/kgf for the classic SRR. Fig. 4(d) presents the induced strain (in microstrain) as a function of operating frequency shift. Here Young's modulus of the cast polyamide beam was taken to be 2.37 GPa, which is separately verified using a wired strain gauge (Tokyo Sokki Kenkyujo Company, Ltd., Strain Gauges with a gauge factor of 2.1). This SRR sensor demonstrates a sensitivity of 0.0259 kHz/microstrain. In Fig. 4(e), we observed that this sensor had less than 500-microstrain nonlinearity errors, which corresponded to 16% nonlinearity error, as shown in Fig. 4(f).

Transmission spectra of our novel SRR structure (nested SRR) for different levels of the applied load are illustrated in Fig. 5(a) and with zoom-in view in Fig. 5(b). Here the operating frequency was 506.2 MHz under no load, which was lower than that of the classical SRR, and a function of an increased number of in the nested SRR. The size of this nested SRR corresponded to $\lambda_o/26.7$. Fig. 5(c) plots the change in the operating frequency with respect to the case of no load as a function of the applied load and indicates a sensitivity of 1.09 kHz/kgf. The sensitivity of the nested SRR was significantly increased compared to the classical SRR as a result of the multiple gaps used in the nested SRR. Fig. 5(d) plots the strain versus frequency shift demonstrating a sensitivity of 0.0369 kHz/microstrain. In Fig. 5(e), the nested SRR sensor had less than 600-microstrain nonlinearity errors, corresponding to less than 16% nonlinearity error in Fig. 5(f). The nonlinearity errors of the nested SRR sensors are nearly the same as those of the classical SRR. However, the nested SRR sensor exhibited reduced operating frequency and increased sensitivity.

B. Biocompatibility Experiments of our Sensors

New Zealand white rabbits (Harlan, Inc., Indianapolis, IN) were chosen as an appropriate animal model to investigate the sit-specific biocompatibility of our MEMS sensors due to their size and ability to house multiple sensor chips. A total of four rabbits each implanted with four sensors and two control material implants (6 implants/rabbit; 16 sensors and 8 controls total) were used to investigate the biocompatibility in accordance with ASTM Standards F981-04 and F763-04. Animals were humanely euthanized six months post-operatively at which time critical gross pathology and microscopic evaluation of the implant sites for an implant-associated tissue reaction was pursued.

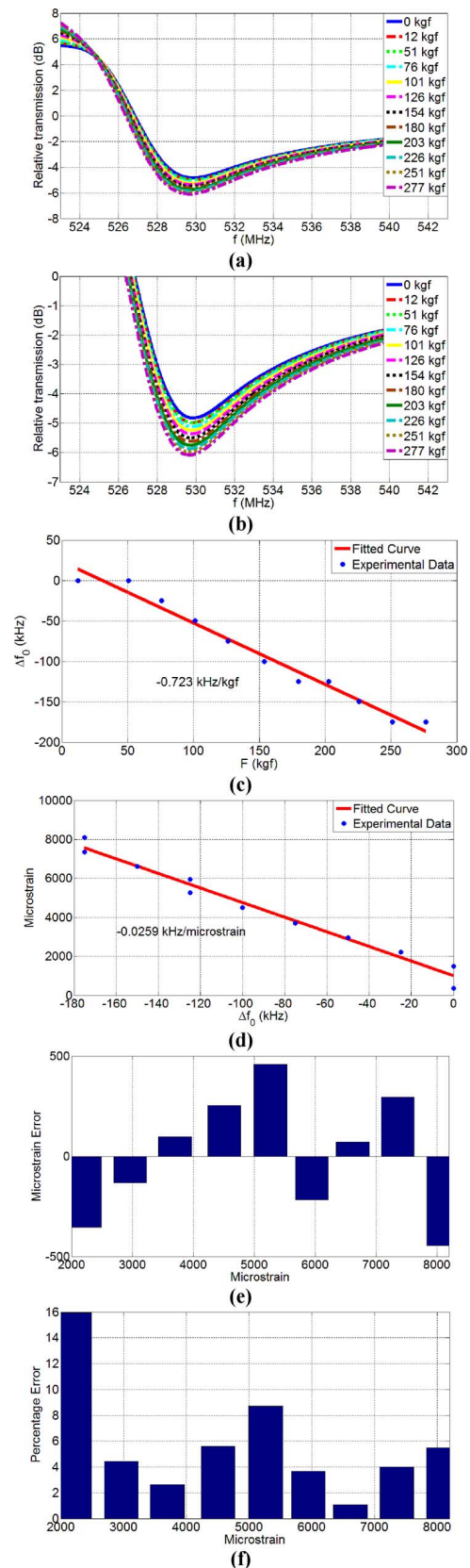


Fig. 4. Experimental characterization of the classical SRR sensor under tension. (a) Relative transmission spectra. (b) Zoom-in view of the transmission shift. (c) Frequency shift (Δf_o) versus applied load (F). (d) Induced strain (microstrain) versus frequency shift (Δf_o). (e) Nonlinearity error (in microstrain). (f) Nonlinearity error percentage.

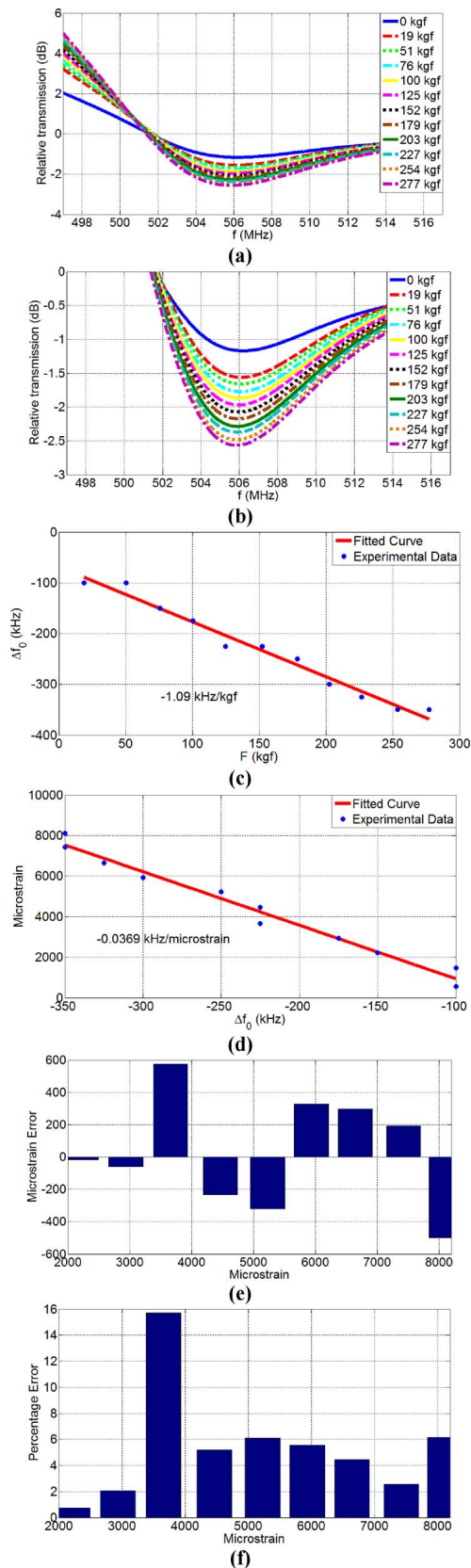


Fig. 5. Experimental characterization of the nested SRR sensor under tension. (a) Relative transmission spectra. (b) Zoom-in view of the transmission shift. (c) Frequency shift (Δf_0) versus applied load (F). (d) Induced strain (microstrain) versus frequency shift (Δf_0). (e) Nonlinearity error (in microstrain). (f) Nonlinearity error percentage.

This study was approved by the Institutional Animal Care and Use Committee (IACUC #07-057A-01) at Colorado State University. New Zealand white rabbits were placed on a constant temperature-heating pad (32–37 °C), and premedicated and sedated with intramuscular acepromazine (1 mg/kg) and anesthetized by inhalation of 4% isoflurane delivered after intubation with a cuffed 3 mm endotracheal tube (Harvard apparatus dual phase control respiratory pump-canine, Harvard Apparatus Company, South Natic, MA). Respiration was accomplished with a tidal volume of 15 mL/kg and frequency of 20–30/min. The peak airway pressure was 20 cm H₂O. Anesthesia was maintained by 1.5% isoflurane.

Prior to surgery, all implant sensors were sterilized terminally via two cycles of autoclave for 25 min/10 min dry at 121 °C. The surgical sites were denuded of all hair on both sides of the spinal column. The skin was swabbed lightly with diluted alcohol and dried prior to sample implantation. Each rabbit received six ($n = 6$) sterilized samples (four test materials and two controls) each implanted in individual sites of the lumbar paravertebral musculature. Two sensor chips (5 mm × 5 mm) and one control specimen (aluminum oxide Al₂O₃; ASTM F603-00) were placed parallel to and on either side of the spinal column approximately 2.5 to 5 cm from midline and 2.5 cm apart from each other, resulting in a total of three implants per side.

Animals were euthanized six months postoperatively by intravenous injection of sodium pentobarbital (150 mg/kg). This method is consistent with the recommendations of the Panel on Euthanasia of the American Veterinary Medical Association. The tissue surrounding and overlying each implant, both for the sensor material and the Al₂O₃ control material, was macroscopically evaluated for evidence of internal and external lesions in accordance with a semiquantitative scoring system developed in our laboratory. Each implant was then removed with an intact envelope (~ 4 mm) of surrounding tissue and fixed for 24 hours in 10% neutral buffered formalin. After fixation, each implant was removed from the tissue envelope, and the tissue specimens were routinely processed, embedded in paraffin, sectioned at 5 μ m, and stained with Hematoxylin and Eosin (H&E) for semiquantitative evaluation of the cellular and tissue response to the sensor and control materials. Microscopic evaluation was performed by a single board certified pathologist who was blinded to the treatment groups so as to avoid observer bias.

The animal surgeries were uneventful and vital signs were normal. During convalescence, there were no complications resulting from the surgical procedure, no evidence of postoperative infection, and no mortality in the six-month survival period. Gross examination of tissue adjacent to these sensor materials did not reveal any visible signs of adverse reactions manifested as external or internal lesions to the test materials. No infection or inflammation was grossly noted in the musculature surrounding implanted materials.

Microscopic examination of the H&E stained slides confirmed that there was no adverse tissue reaction to the sensor materials either immediately adjacent to or peripheral to the implantation site, as shown in Fig. 6. Examination of histological slides confirmed the absence of abnormal macrophage or

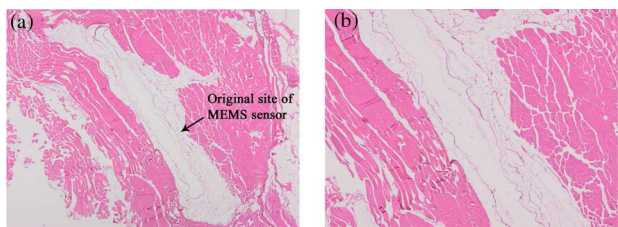


Fig. 6. (a) $2\times$ and (b) $4\times$ images of the H&E stained tissue adjacent to the implanted sensor. After six months *in vivo*, no evidence of inflammation or adverse tissue response was documented adjacent to any of the implanted sensors demonstrating adequate biocompatibility.



Fig. 7. *In vitro* characterization with soft tissue in (a) front view showing antennas and (b) back view showing the sensor.

lymphocytic cellular activity. As a result, inflammation scores for the sensor and Al_2O_3 control materials were 0 ± 0 and 0 ± 0 (mean \pm standard deviation), respectively. Minimal fibrosis was noted, surrounding both the control and sensor materials (1.0 ± 0.5 and 0.94 ± 0.24 , respectively), and the general toxicity score for the test and control materials was zero.

C. Soft Tissue Experiments

After showing enhanced functional performance with the nested SRR sensor relative to the classic SRR design and demonstrating biocompatibility of our sensors, we investigated the fidelity with which we could detect the shift in transmission spectra in a scenario that more closely resembles the intended application of the device: one in which soft tissue separates the sensor and the antennae, as would be the case while monitoring bending strains on internal hardware in human patients [see Fig. 7(a) and (b)]. Fig. 8(a) and (b) depicts the transmission spectra of the nested SRR with the soft tissue parameterized with respect to the applied load. In the soft tissue experiment, the operating frequency of the nested SRR was 474.2 MHz under no load, which was lower than that measured in free space (see Fig. 5). This is an exact consequence of the soft tissue, as it has a very high dielectric constant of 56.445 around 500 MHz [30], thereby decreasing the resonance frequency of the device. The sensitivity of the sensor [see Fig. 8(c)] under these test conditions was also increased to 4.00 kHz/kgf because the soft tissue better focuses on electromagnetic waves compared to the free space because of its high dielectric constant at low frequencies. Consequently, the mechanical deformation under load affects the operating frequency more strongly, which leads to better sensitivity in the soft tissue.

Using the soft tissue medium is advantageous for our sensing application since the operating frequency is lowered. It should be noted that the space between the antennae and soft tissue should

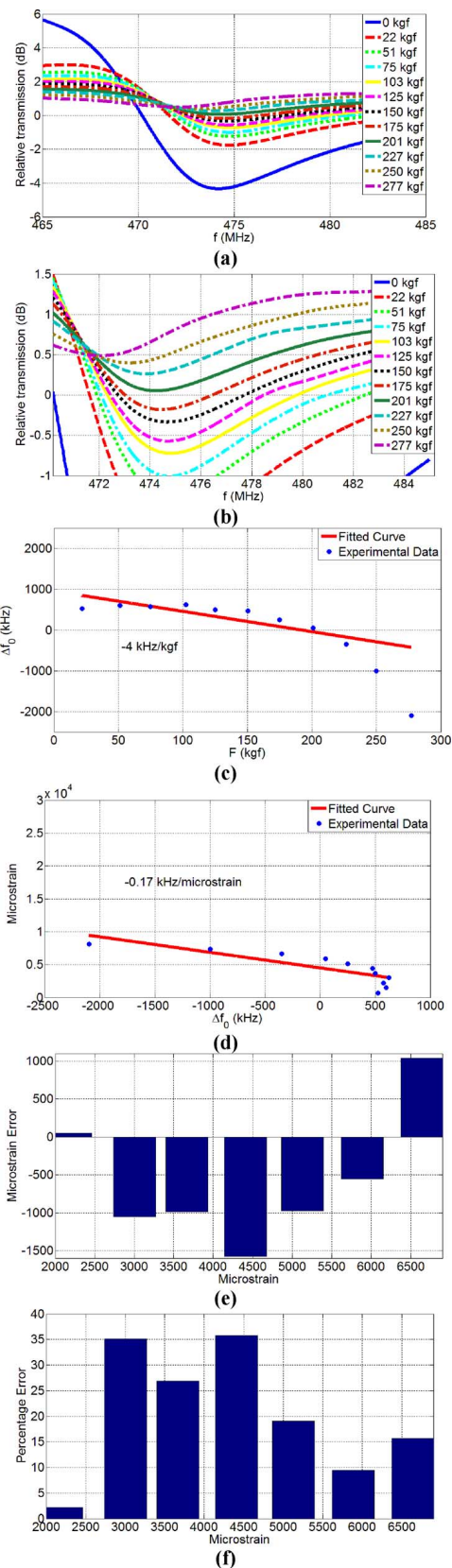


Fig. 8. Experimental characterization of the nested SRR sensor using soft tissue under tension. (a) Relative transmission spectra. (b) Zoom-in view of the transmission shift. (c) Frequency shift (Δf_0) versus applied load (F). (d) Induced strain (microstrain) versus frequency shift (Δf_0). (e) Nonlinearity error (in microstrain). (f) Nonlinearity error percentage.

be kept at an absolute minimum. If there is sufficient free space between them, then the antenna signal decreases dramatically. Also, in Fig. 8(d), we show the strain versus operating frequency shift and obtain 0.17 kHz/microstrain sensitivity. In Fig. 8(e), the nested SRR sensor had a maximum of 1500-microstrain nonlinearity errors, corresponding to 35% nonlinearity error, as shown in Fig. 8(f), in the soft tissue, which is larger than in the free space. We are currently working on understanding the nonlinearity error sources.

IV. CONCLUSION

In conclusion, we designed, fabricated, and characterized a novel nested SRR for implant strain sensing. We demonstrated that the nested SRR sensor outperforms the classical SRR sensor with regard to operating frequency and sensitivity, which was a direct result of the increased number of gaps in the nested architecture. The unloaded operating frequency of nested SRR (506.2 MHz) was decreased relative to the classical SRR (529.8 MHz) in the free-space experiments. Further, the sensitivity of the nested SRR (1.09 kHz/kgf) was increased with respect to the classical SRR (0.72 kHz/kgf) in the free space.

We also demonstrated biocompatibility of our metamaterial sensors by implanting them into New Zealand white rabbits and observing no evidence of inflammation or adverse tissue response over a period of six months. As a first proof-of-concept demonstration using soft tissue in a situation that approximates the clinical condition, we demonstrated that the unloaded operating frequency and sensitivity of the nested sensor were 474.2 MHz and 4.00 kHz/kgf, respectively. These findings were a direct consequence of the interposed soft tissue, which exhibits a very high dielectric constant and effectively served to better focus on the incident electromagnetic waves. The results presented herein support the continued development and characterization of a fracture healing system based on these implantable metamaterial sensors with nested architecture.

ACKNOWLEDGMENT

We would like to thank to K. B. Alici for his help in making our external antenna.

REFERENCES

- [1] K. Stoffel, K. Klaue, and S. M. Perren, "Functional load of plates in fracture fixation *in vivo* and its correlate in bone healing," *Injury*, vol. 31, pp. 37–50, 2000.
- [2] J. D. Heckman and J. Sarasohn-Kahn, "The economics of treating tibia fractures. The cost of delayed unions," *Bull. Hosp. Joint Dis.*, vol. 56, pp. 63–72, 1997.
- [3] E. W. Lambert, R. B. Simpson, A. Marzouk, and D. V. Unger, "Orthopaedic injuries among survivors of USS COLE attack," *J. Orthop. Trauma*, vol. 17, pp. 436–441, 2003.
- [4] M. S. Gaston and A. H. Simpson, "Inhibition of fracture healing," *J. Bone Joint Surg. Br.*, vol. 89, pp. 1553–1560, 2007.
- [5] A. H. Simpson, T. N. Gardner, M. Evans, and J. Kenwright, "Stiffness, strength, and healing assessment in different bone fractures—a simple mathematical model," *Injury*, vol. 31, pp. 777–781, 2000.
- [6] J. Webb, G. Herling, T. Gardner, J. Kenwright, and A. H. Simpson, "Manual assessment of fracture stiffness," *Injury*, vol. 27, pp. 319–320, 1996.
- [7] G. M. Kotzar, D. T. Davy, J. Berilla, and V. M. Goldberg, "Torsional loads in the early postoperative period following total hip replacement," *J. Orthop. Res.*, vol. 13, pp. 945–955, 1995.
- [8] G. M. Kotzar, D. T. Davy, V. M. Goldberg, K. G. Heiple, J. Berilla, Jr., K. G. Heiple, R. H. Brown, and A. H. Burstein, "Telemeterized *in vivo* hip joint force data: A report on two patients after total hip surgery," *J. Orthop. Res.*, vol. 9, pp. 621–633, 1991.
- [9] D. T. Davy, G. M. Kotzar, R. H. Brown, K. G. Heiple, V. M. Goldberg, K. G. Heiple, J. Berilla, and A. H. Burstein, "Telemetric force measurements across the hip after total arthroplasty," *J. Bone Joint Surg. Am.*, vol. 70, pp. 45–50, 1998.
- [10] A. Rohlmann, F. Graichen, R. Kayser, A. Bender, and G. Bergmann, "Loads on a telemeterized vertebral body replacement measured in two patients," *Spine*, vol. 33, pp. 1170–1179, 2008.
- [11] A. Rohlmann, F. Graichen, and G. Bergmann, "Loads on an internal spinal fixation device during physical therapy," *Phys. Ther.*, vol. 82, pp. 44–52, 2002.
- [12] A. Rohlmann, F. Graichen, U. Weber, and G. Bergmann, "2000 Volvo Award winner in biomechanical studies: Monitoring *in vivo* implant loads with a telemeterized internal spinal fixation device," *Spine*, vol. 25, pp. 2981–2986, 2000.
- [13] S. J. Taylor and P. S. Walker, "Forces and moments telemetered from two distal femoral replacements during various activities," *J. Biomech.*, vol. 34, pp. 839–848, 2001.
- [14] S. J. Taylor, P. S. Walker, J. S. Perry, S. R. Cannon, and R. Woledge, "The forces in the distal femur and the knee during walking and other activities measured by telemetry," *J. Arthroplasty*, vol. 13, pp. 428–437, 1998.
- [15] W. E. Kock, "Metal-lens antennas," *Proc. IEEE*, vol. 34, pp. 828–836, 1946.
- [16] V. G. Veselago, "The electrodynamics of substances with simultaneously negative values of epsilon and mu," *Usp. Fiz. Nauk*, vol. 92, pp. 517–526, 1967.
- [17] R. M. Walser, *Introduction to Complex Mediums for Electromagnetics and Optics*. Bellingham, WA: SPIE, 2003.
- [18] D. R. Smith, "The reality of negative refraction," *Phys. World*, vol. 16, pp. 23–24, 2003.
- [19] D. R. Smith, J. B. Pendry, and M. C. K. Wiltshire, "Metamaterials and negative refractive index," *Science*, vol. 305, pp. 788–792, 2004.
- [20] V. M. Shalaev, W. Cai, U. K. Chettiar, H.-K. Yuan, A. K. Sarychev, V. P. Drachev, and A. V. Kildishev, "Negative index of refraction in optical metamaterials," *Opt. Lett.*, vol. 30, pp. 3356–3358, 2005.
- [21] V. M. Shalaev, "Optical negative-index metamaterials," *Nature Photon.*, vol. 1, pp. 41–48, 2007.
- [22] V. A. Podolskiy, A. K. Sarychev, and V. M. Shalaev, "Plasmon modes in metal nanowires and left-handed materials," *J. Nonlinear Opt. Phys. Mater.*, vol. 11, pp. 65–74, 2002.
- [23] K. B. Alici and E. Ozbay, "Electrically small split ring resonator antennas," *J. Appl. Phys.*, vol. 101, pp. 083104-1–083104-4, 2007.
- [24] J. B. Pendry and S. A. Ramakrishna, "Focusing light using negative refraction," *J. Phys. [Condensed Matter]*, vol. 15, pp. 6345–6364, 2003.
- [25] D. Schurig, J. J. Mock, B. J. Justice, S. A. Cummer, J. B. Pendry, A. F. Starr, and D. R. Smith, "Metamaterial electromagnetic cloak at microwave frequencies," *Science*, vol. 314, pp. 977–980, 2006.
- [26] D. R. Smith, "How to build a superlens," *Science*, vol. 308, pp. 502–503, 2005.
- [27] R. Melik, E. Unal, C. Puttlitz, and H. V. Demir, "Wireless metamaterial RF-MEMS strain sensors," *Appl. Phys. Lett.*, vol. 95, pp. 011106-1–011106-3, 2009.
- [28] R. Melik, N. K. Perkgoz, E. Unal, Z. Dilli, and H. V. Demir, "Design and realization of a fully on-chip high-Q resonator working at 15 GHz on silicon," *IEEE Trans. Electron Devices*, vol. 55, no. 12, pp. 3459–3466, Dec. 2008.
- [29] R. Melik, N. K. Perkgoz, E. Unal, C. Puttlitz, and H. V. Demir, "Bio-implantable passive on-chip strain sensors for the assessment of bone fractures," *J. Micromech. Microeng.*, vol. 18, no. 11, pp. 115017-1–115017-9, 2008.
- [30] [Online]. Available: <http://niremf.ifac.cnr.it/tissprop/htmlclie/htmlclie.htm>

Rohat Melik (S'07) was born on Jan. 29, 1982 in Diyarbakir, Turkey. He graduated from Sanliurfa Anatolian High School and from Ankara Science High School, Ankara. He received the B.Sc. degree from the Department of Electrical and Electronics Engineering and Department of Economics (Minor in International Economics) from Middle East Technical University, Ankara, in 2004. He is currently working toward the Ph.D. degree in electrical and electronics engineering with Nanotechnology Research Center and Institute of Materials Science and Nanotechnology, Bilkent University, Ankara under the supervision of Prof. H. V. Demir.

His research interests include bioimplant RF-MEMS devices and sensors, including the design, fabrication, and characterization of these components at Bilkent University.

Emre Unal received the B.Sc. degree in electrical and electronics engineering from Hacettepe University, Ankara, Turkey, in 2005.

He is currently a full-time Research Engineer with Nanotechnology Research Center and Institute of Materials Science and Nanotechnology, Bilkent University, Ankara, under the supervision of Prof. H. V. Demir. His research interests include the development of microwave and optoelectronic devices at Bilkent University.

Nihan Kosku Perkgoz received the B.Sc. degree in electrical and electronics engineering from Middle East Technical University, Ankara, Turkey, in 1999, and the M.S. and Ph.D. degrees in semiconductor electronics and integrated science from Hiroshima University, Hiroshima, Japan, in 2003 and 2005, respectively.

In April 2007, she was a Postdoctoral Research Fellow and Projects Coordinator in the Demir Devices and Sensors Research Group, Nanotechnology Research Centre, and Institute of Materials Science and Nanotechnology, Bilkent University, Ankara. Her current research interests include RF and optoelectronic devices.

Brandon Santoni received the B.S. degree in microbiology and biochemistry from Texas Tech University, Lubbock, in 1998, and the M.S. and Ph.D. degrees in mechanical engineering from Colorado State University, Fort Collins, in 2003 and 2006, respectively.

He is currently a Research Scientist in the Orthopedic Bioengineering Research Laboratory, Department of Mechanical Engineering and School of Biomedical Engineering, Colorado State University. His research interests include bone biology, regeneration, and healing, as well as orthopedic biomechanics.

Debra A. Kamstock received the D.V.M. degree from the University of Florida, Gainesville and the Ph.D. degree in pathology from Colorado State University, Fort Collins.

In 2007, she was a Diplomate of the American College of Veterinary Pathologists, where she specialized in anatomic pathology. She is currently an Assistant Professor with the Orthopedic Bioengineering Research Laboratory, Department of Mechanical Engineering and School of Biomedical, Colorado State University. Her research interests include oncological pathology, with emphasis in carcinogenesis, tumor angiogenesis, tumor immunology, and cancer vaccines.

Christian Puttlitz received the B.S. degree in materials science and mechanics from Michigan State University, East Lansing, in 1992, the M.S. degree in bioengineering from Clemson University, Clemson, SC, in 1993, and the Ph.D. degree in biomedical engineering from the University of Iowa, Iowa City, in 1999.

From 1999 to 2001, he was a Postdoctoral Research Fellow in orthopedic biomechanics with the University of California, San Francisco (UCSF). In May 2001, he was an Assistant Professor in the Department of Orthopedic Surgery at the UCSF and Director of the Orthopedic Biomechanics Laboratory at the San Francisco General Hospital, San Francisco, CA. In August 2004, he was a Faculty Member with the Department of Mechanical Engineering, Colorado State University (CSU), Fort Collins, where he is currently an Associate Professor and Head of the Orthopedic Bioengineering Research Laboratory. His current research interests include experimental and computational investigations in orthopaedic biomechanics as it relates to normal function, disease states, and treatments.

Hilmi Volkan Demir (S'97–M'04) received the B.Sc. degree in electrical and electronics engineering from Bilkent University, Ankara, Turkey, in 1998, and the M.S. and Ph.D. degrees in electrical engineering from Stanford University, Stanford, CA, in 2000 and 2004, respectively.

Since 2004, he has been a Faculty Member with Bilkent University, with joint appointments at the Department of Electrical and Electronics Engineering and the Department of Physics. He is the Principle Investigator of the Devices and Sensors Laboratory and the Associate Director of Nanotechnology Research Center, Bilkent University. He also received the Docent title (Associate Professor) from Turkish Council of Higher Education, in 2007. His current research interests include the development of innovative optoelectronic devices and novel bioimplant RF devices.

Dr. Demir received the European Union Marie Curie Fellowship in 2005, the Turkish National Academy of Sciences Distinguished Young Scientist Award in 2006, and the European Science Foundation European Young Investigator Award in 2007.